Dependency of Portevin-LeChatelier Effect and Microstructure Characteristics of 9Cr ODS Steels on Strain Rates Upon Hot Deformation

Xiaosheng Zhou[1] · Yaran Zhang[2] · Yanmo Li[3] · Meini Yuan[4] · Guodong Li[1] · ZhenYa Chen[1] · Huang Zhang[1]

Abstract

The flow stress and microstructure evolution of 9Cr oxide dispersion strengthened (ODS) steels were investigated by isothermal compression at 1000–1150 ºC with strain rates from 0.001 to 1 s^{-1}. Microstructure characteristics of ODS steels under various condition were studied using the EBSD and TEM techniques. At each deformation temperature, PortevinLe-Chatelier (PLC) effect characteristics of repeated serrated stress was observed, as the strain rates were 0.01, 0.1 and 1 s^{-1}. The serrations fluctuated about the mean flow curve in quick succession, and the critical strain for the PLC effect was related to both the deformation temperature and strain rates. The stress drops at strain rates of 0.01 and 0.1 s^{-1} were smaller than those at 1 s^{-1}. The strain rate affected the dynamic recovery and recrystallization of austenite grains, as well as the texture components of martensite transformed from austenite. Cap-shaped oxide particles in as-fabricated and hot deformed steels were characterized in detail. The cap parts of cap-shaped oxide particles were depleted of alloying elements, and the caps were crystal or amorphous. Large-sized oxide particles were easier to be deformed than small-sized ones. Despite of the oxide deformation, the PLC effect was still suggested to be related to the solute-dislocation interaction.

Keywords Oxide nanoparticles · Portevin-LeChatelier effect · Element distribution · Texture · Oxide deformation

1 Introduction

Nuclear energy has been one promising choice to satisfy increasing energy demands, owing to its advantages in fuel economy and environmental protection [1]. To ensure the safety operation of nuclear reactors, the structural materials should exhibit favorable high-temperature strength, good radiation resistance and corrosion resistance [2]. By introducing high density of oxide nanoparticles into ferritic/

✉ Xiaosheng Zhou
zhouxs@nuc.edu.cn

1. Shanxi Key Laboratory of Intelligent Equipment Technology in Harsh Environment, School of Mechanical Engineering, North University of China, 030051 Taiyuan, China

2. Material Science Research Center, Xingtai University, Xingtai 054001, China

3. Luoyang Ship Material Research Institute, Luoyang 471023, China

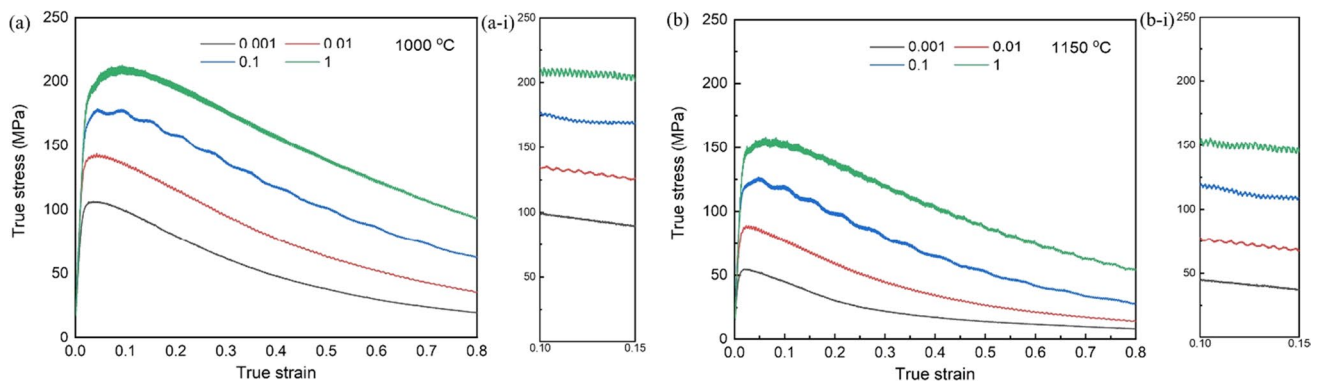4. College of Mechatronic Engineering, North University of China, Taiyuan 030051, China

martensitic (F/M) steels through powder metallurgy, the oxide dispersion strengthened (ODS) steels obtain superior service performance to conventional F/M steels, and can be used as fuel cladding tubes for fast reactors or blanket structure for fusion reactors [3, 4]. The fabrication of ODS steels usually involves mechanical milling, hot consolidation (hot extrusion, hot isostatic pressing or spark plasma sintering) and post-heat treatment, and based on the alloying composition and matrix microstructure, they can be classified into ferritic ODS steels, martensitic ODS steels and ferritic-martensitic dual-phase steels [5–7].

Metallurgical changes occur during consolidation process of steels and alloys, and the resultant microstructure will affect the mechanical properties significantly [8]. Thermomechanical treatments are essential for the production of complex components made of ODS steels. Continuous dynamic recrystallization was responsible for the for the grain refinement in the 18Cr ferritic ODS steels, and considerable coarsening of nanoprecipitates with bimodal particle distribution was revealed as the deformation temperature reached to 1300 ºC [9]. It was suggested that precipitate density not only affected the intragranular dislocation glide

Fig. 1 True stress-strain curves of 9Cr ODS steels deformed at different **a** 1000 °C and **b** 1150 °C. For clarity, **a**–i and **b**–i respectively shows the enlarged parts at the strains from 0.1 to 0.15

activity, but also reduced the kinetics of continuous dynamic recrystallization in coarse grains of ODS steels [10]. Instability of flow stress can also be observed upon the hot deformation, and it is often reported in structural and functional materials like metallic glass, superalloys, carbon steels, Al-Mg alloys and so on [11]. In several studies on the hot deformation behavior of ODS steels, although discontinuous stress flow curves were exhibited, the discussion on these serrated flows was not concerned. These studies were just focused on microstructural evolution during hot deformation and the processing map of ODS steels [9, 12–14]. From an engineering point of view, metal forming processes should be conducted outside the regimes of plastic instabilities, in order to avoid ductility loss and deformation inhomogeneities (stretcher strains) [15]. Thus, it is necessary to further explore the critical conditions of serrated flow in ODS steels. In this work, the characteristics of flow instability in 9Cr ODS steels upon hot deformation are studied in detail. Since the flow instability is sensitive to the strain rate, the effects of strain rates on the microstructural evolution of ODS steels are also investigated, attempting to better understand the underlying mechanism of flow instability in ODS steels.

2 Experimental

Pre-alloyed powders with the nominal composition of Fe-9Cr-0.1 C-2 W-0.2 V-0.07Ta (wt%) were prepared by inert gas atomization, and then blended with commercial 0.35 wt% Y_2O_3 powders with sizes smaller than 30 nm. The mixed powders were mechanical alloyed in a planetary ball mill at a rotation speed of 400 rpm for 45 h, with Ar as the protection atmosphere. The ball to powder ratio was 15:1, and the milling media was stainless steel balls. Milled powders were consolidated by hot isostatic pressing (HIP) at 1150 °C for 3 h under a pressure of 150 MPa. The as-HIPed 9Cr ODS steel was machined into samples with size

of $\Phi 8 \times 12$ mm for hot deformation. The hot deformation was performed on a Gleeble-1500 simulator at temperatures of 1000, 1050, 1100 and 1150 °C with strain rates from 0.001 to 1 s^{-1}. The samples were quenched in water after the hot deformation.

The microstructure characteristics was examined using scanning electron microscopy (SEM) equipped with electron back-scattered diffraction (EBSD) and transmission electron microscopy (TEM). For microstructure examination, deformed specimens were sectioned along the axis of compressive direction. A step size of 0.15 μm was used in EBSD characterization. Grain orientations and local texture were respectively characterized by inverse pole figure (IPF) maps and orientation distribution function (ODF) sections. TEM specimens were chipped by ion milling (Gatan 691), and high-resolution TEM (HRTEM) was used to reveal the lattice of oxide nanoparticles. During ion milling, the samples were ion thinned at 6°/ 5Kev for 50 min, then thinned at 4°/ 4Kev for 50 min, and finally thinned at 3°/ 3Kev for 50 min.

3 Results and Discussion

3.1 Portevin-LeChatelier Effects

Figure 1a and b respectively show the true stress-strain curves of the ODS steels deformed at 1000 and 1150 °C with various strain rates. For each deformation temperature, the hot deformation behaviors of ODS steels exhibit similar characteristics. The stress first rapidly increases with strain until to one peak stress, and then gradually decreases with strain. With respect to the steel deformed at 1150 °C with the strain rate of 0.001 s^{-1}, the flow stress curve is composed of work hardening stage, softening stage and steady stage. During the hot deformation, dynamic recovery (DRV) and dynamic recrystallization (DRX) occur simultaneously. At the initial stage, the working hardening overwhelms the
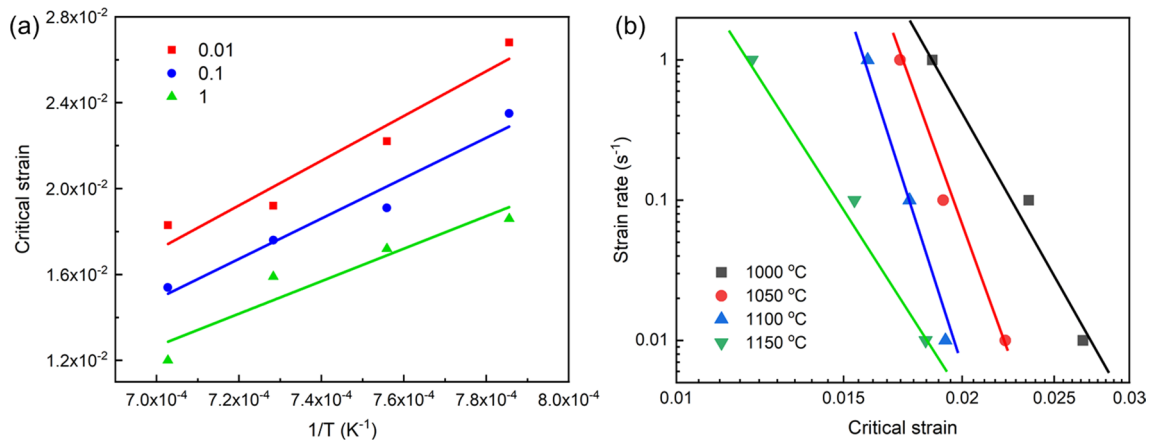
Fig. 2 a Dependency of critical strain on temperature at various strain rates and **b** the variation of critical strain with strain rates at temperatures

dynamic softening mechanism (including DRV and DRX), and the flow stress increases. When the strain reaches the peak strain, the dynamic softening caused by dynamic recrystallization starts to outweigh the work hardening. Then, the flow stress gradually decreases. As the work hardening and dynamic softening becomes balanced, the stress remains steady [16].

Figure 1 (a–i) and (b–i) respectively show the enlarged parts of the Fig. 1a and b at the strains from 0.1 to 0.15, revealing more deformation details. For the strain rates of 0.01, 0.1 and 1 s^{-1}, repeated "jerks" or "serrations" are throughout the entire regime, which is the predominant feature of Portevin–LeChatelier (PLC) effect. PLC effects of 9Cr ODS steels are sensitive to the strain rates, but not to the deformation temperature. For each deformation temperature, the PLC effect can only be observed at the strain rates of 0.01, 0.1 and 1 s^{-1}. In general, serrations associated with the PLC effect can be classified into type A, type B and type C. Type A serrations rise above the stress envelope at their onset, and exhibits sparse serrations and small stress drops. Type B serrations fluctuate about the mean flow curve in quick succession. Type C serrations fall below the stress envelope with large stress decrement. With increase in temperature or decrease in strain rate, serration type changes from type A to type B, and then to type C [17, 18]. The serration density generally exhibits the following relationship: type B > type C > type A. In this case, the involved serrations all belong to type B.

Serrated flow stress initiates after a critical strain. If the critical strain increases with the increase in strain rate or the decrease in temperature, the flow stress is defined as normal PLC effect. If the critical strain increases with the decrease in strain rate or the increase in temperature, the stress behavior is called inverse PLC effect [19]. Figure 2a shows the dependency of critical strain on temperature at various strain rates, which shows that ODS steels exhibit

normal PLC effect. However, in Fig. 2b showing the variation of critical strain with strain rates at various temperatures, characteristics of inverse PLC effect are observed.

Dynamic stain aging (DSA) is generally acknowledged to be responsible for the PLC effect. Mobile dislocation temporarily locked at localized obstacles is pinned by diffusing solute atoms. With the flow stress increasing, the dislocation breaks away from the pinning, accompanying with a stress drop. When the pinning and un-pinning of dislocations repeatedly occurs, the stress exhibits PLC effect. In this case, the waiting time for dislocations locked at obstacles should be comparable to the time of solutes diffusing to these dislocations. The critical strain could produce critical concentration of vacancies, promoting the diffusion of solute atoms to mobile dislocations, contributing to the DSA [11]. If the solute diffusion time was well below the waiting time of dislocations at obstacles, the interaction between solute atoms and the locked dislocations could still last upon free flights of dislocation between obstacles, and then the flow stress was free of discontinuous yielding. The PLC effect was not exhibited [20]. Shearing of precipitates by dislocations could also affect the serration behavior. The repetition of precipitate shearing and subsequent stress-relaxation would lead to successive stress drops and visible serrations [11, 21]. Kumar suggested that the inverse PLC effect in Al-Mg alloys was not related to the precipitate shearing, but still related to the solute-dislocation interaction at test temperatures [22].

Although the normal PLC effect has been well modeled, the inverse PLC effect has not been well understood. For the Ni-based alloy at 350 $^{\circ}$C, with the strain rate decreasing, the critical strain had an reversion from the normal PLC effect to the inverse PLC effect [17]. For an Al-4.4%Mg alloy deformed at constant strain rates, with the temperature increasing, the normal PLC effect transformed to the inverse effect [15]. In this work, the critical strain decreases with the temperature increasing. The increase in

Fig. 3 SEM images of the ODS steels deformed under **a** 1000 ^{o}C/1 s^{-1} and **b** 1150 ^{o}C/0.001 s^{-1}

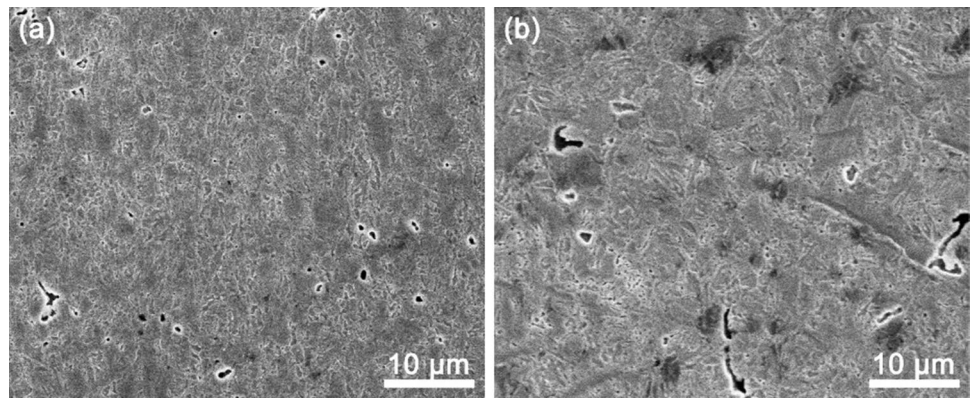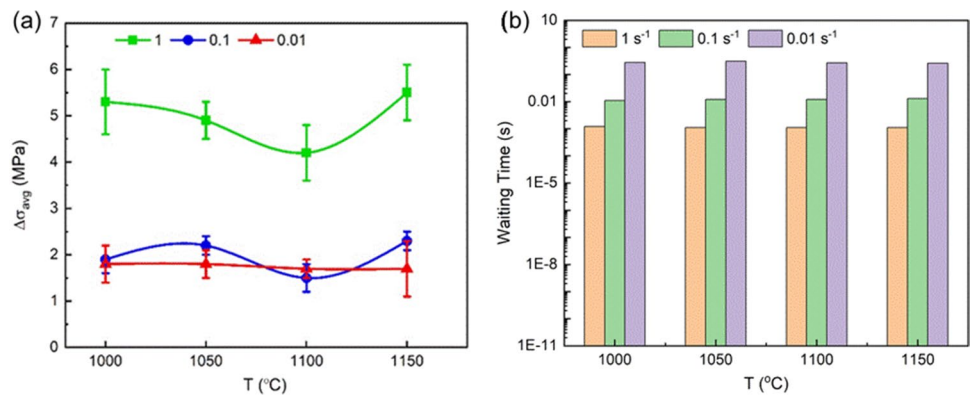**Fig. 4** **a** Variation of average stress decrement, $\Delta\sigma_{avg}$, with temperature, T, at different strain rates; **b** waiting time of dislocations at obstacles at various strain rates and temperature

temperature enhances the thermal diffusion of pinning solutes, and then the critical vacancy concentration facilitating solute diffusion can be lowered, as well as the critical strain. The dependency of the critical strain on strain rates in this work can be explained as follows. High density of non-shearable oxide nanoparticles are present in ODS steels. During compressive deformation, due to the incompatible deformation between the oxide nanoparticles and matrix, nanoscale voids can be formed at their interface [23]. For one certain time, the incompatible deformation between the oxide nanoparticles and matrix is enhanced with the strain rate increasing, and nanoscale voids should be easier produced. The nanoscale voids could further facilitate the diffusion of solute atoms, leading to the decrease in the critical strain for DSA. Figure 3a and b respectively show the SEM images of the steels deformed under 1000 ^{o}C/1 s^{-1} and 1150 ^{o}C/0.001 s^{-1} conditions. The steel deformed under 1000 ^{o}C/1 s^{-1} shows higher density of voids than that under 1150 ^{o}C/0.001 s^{-1}, but the void size is smaller. The lager void size at 1150 ^{o}C/0.001 s^{-1} should be related to the coarsening of oxide nanoparticles under this condition.

Figure 4a shows the variation of the averaged stress drop with the deformation temperature at various strain rates. For the strain rates of 0.1 and 1 s^{-1}, the stress drop generally decreases with the deformation temperature increasing until

to 1100 ^{o}C, and then increases at 1150 ^{o}C. At 0.01 s^{-1}, the deformation temperature has a negligible effect on the stress drops. For the strain rates of 0.01 and 0.1 s^{-1}, the stress drops change irregularly. However, the stress drops at these two strain rates are smaller than those at 1 s^{-1}. The magnitude of stress drops indicates the pinned strength of dislocations by solutes [24]. It was reported that the stress drop generally increased with the strain rate decreasing and the temperature increasing [17, 25]. In this work, effects of strain rates and temperature on stress drops are different from these reported results. The strength of dislocations pinned by solute atoms is affected by the waiting time at obstacles and the diffusion of solute atoms towards dislocations. In this work, oxide nanoparticles and forest dislocations act as the obstacles for moving dislocations. Generally speaking, with the strain rate increasing, the waiting time spent on obstacles is decreased, as shown in Fig. 4b. The stress drops at 1 s^{-1} are quite larger than those at 0.01 and 0.1 s^{-1}, although the waiting time at 1 s^{-1} is smaller than those at 0.01 and 0.1 s^{-1}. This indicates that the diffusion of solutes is significantly enhanced at 1 s^{-1}. For one certain strain rate, the waiting times at various temperatures are approximately the same. For the strain rates of 0.01 and 0.1 s^{-1}, temperature has a negligible effect on the stress drops. At 1 s^{-1}, the effects of temperature on the stress drop are more pronounced. With
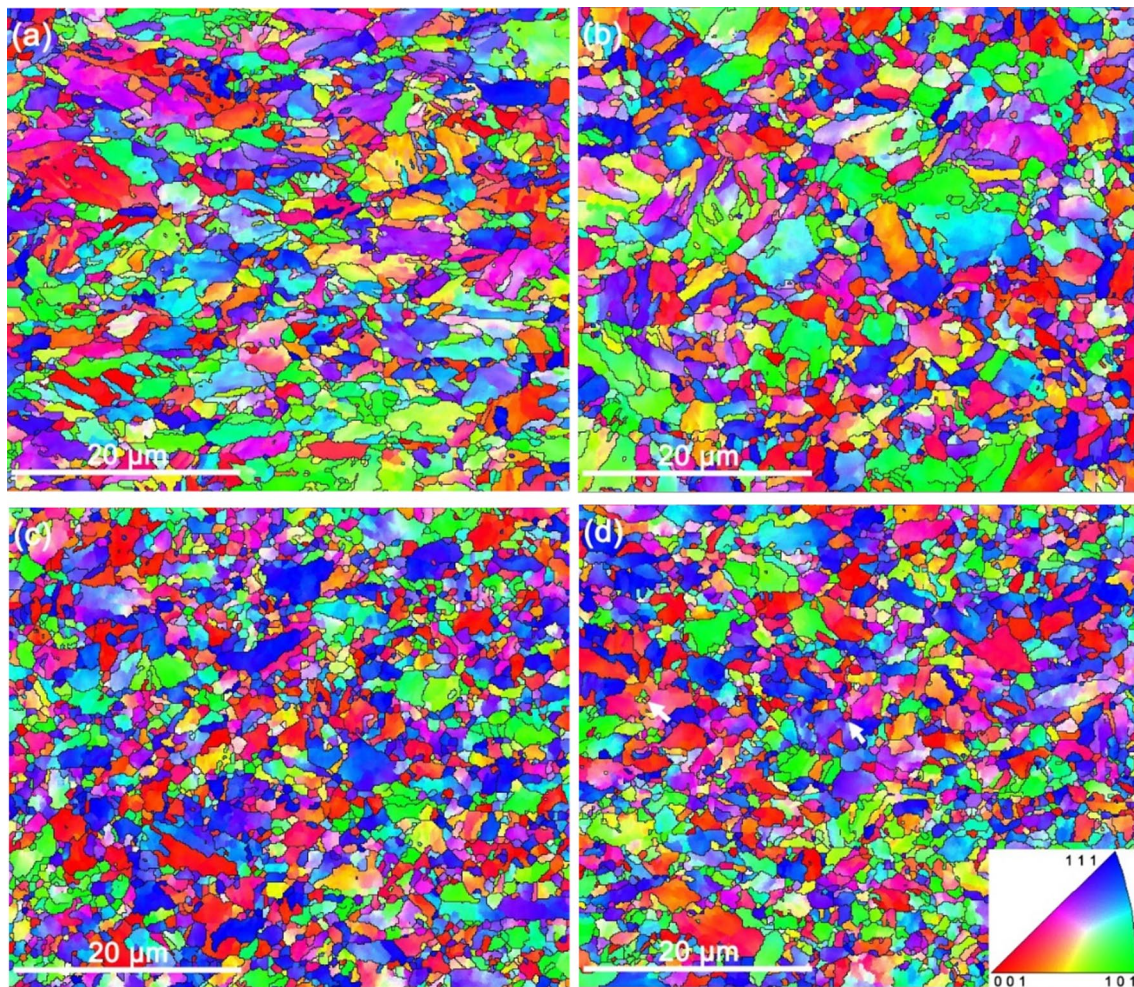
Fig. 5 Grain boundaries (> 15°) coupled with IPF images of ODS steels deformed at 1100 °C for **a** 1 s^{-1}, **b** 0.1 s^{-1}, **c** 0.01 s^{-1} and **d** 0.001 s^{-1}, with respect to compressive direction

the temperature increasing, the thermal diffusion of solutes is enhanced. On the other hand, the dislocation density is decreased, and the vacancy population will also be affected, weakening the vacancy diffusion. Thus, temperature has a complicated effect on the stress drops.

3.2 Local Texture Evolution

Figure 5 shows the IPF images of ODS steels deformed at 1100 °C for different strain rates, as well as the grain boundaries (> 15°). The lath morphology of martensite is not exhibited. It can be seen that strain rates have significant effects on the microstructure of ODS steels. Elongated grains typical of a deformation induced microstructure is evident at 1^1. At 0.1 s^{-1}, the banded structure is not as evident as that at 1 s^{-1}, indicating that dynamic recovery is enhanced at 0.1 s^{-1}. When the strain rates are decreased to 0.01 s^{-1} and 0.001 s^{-1}, equiaxed grains with sizes smaller than 1 µm are prevailing, suggesting that dynamic recrystallization is

the key mechanism at these two strain rates. Recrystallized grains usually nucleated at triple junctions, occasionally within grains, as indicated by white arrows in Fig. 5d. It should be noted that when the size of prior austenite grain is quite small, the entire austenite grain only exhibits one martensite variant.

Figure 6 shows the inverse pole figures intensity distribution corresponding to the same 4 regions shown in Fig. 5, which is beneficial to reveal the texture evolution during hot compression. With respect to the compressive direction, at 1 s^{-1}, $<1\ 1\ 2>_\alpha$ is preferred to it. At 0.1 s^{-1}, the preferential crystallographic directions are close to $<0\ 0\ 1>_\alpha$ and $<1\ 1\ 1>_\alpha$. At 0.01 s^{-1}, both $<0\ 0\ 1>_\alpha$ and $<1\ 1\ 1>_\alpha$ directions are parallel to the compressive axis, while at 0.001 s^{-1}, the intensity of $<0\ 0\ 1>_\alpha$ is decreased significantly. It was reported that when the strain rate of non-transformable 18Cr ODS steels decreased from 10 to 0.01 s^{-1}, the fiber texture along $<1\ 1\ 0>_\alpha$ changed to predominantly $<1\ 0\ 0>_\alpha$. Shearing and partial recrystallization contributed to the

Fig. 6 Inverse pole figures intensity distributions of ODS steels deformed at 1100 °C for **a** 1 s^{-1}, **b** 0.1 s^{-1}, **c** 0.01 s^{-1} and **d** 0.001 s^{-1}, with respect to compressive direction
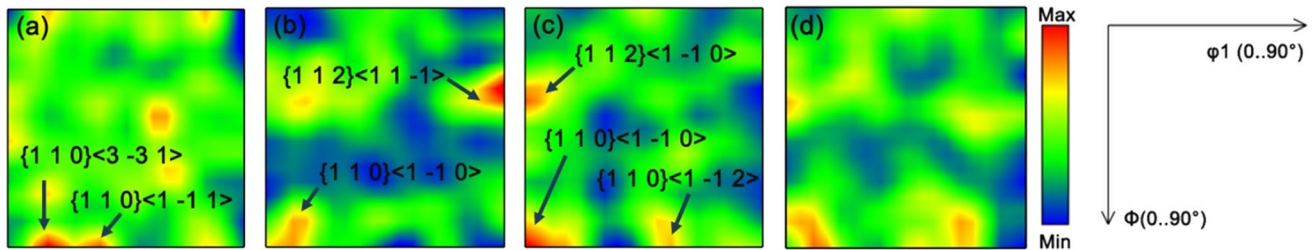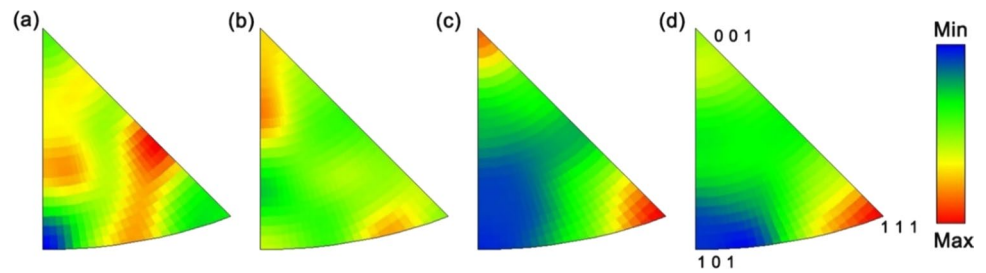
Fig. 7 ODF sections ($\varphi_2 = 45°$) of the longitudinal sections of the specimens deformed at 1100 °C with strain rates of **a** 1 s^{-1}, **b** 0.1 s^{-1}, **c** 0.01 s^{-1} and **d** 0.001 s^{-1}

development of double fiber texture upon plastic deformation [13]. In this study, austenite transformation occurs under the hot deformation conditions, then the austenite transforms into martensite. According to the K-S orientation relationships between austenite and martensite ($\{1\,11\}_\gamma//\{0\,11\}_\alpha$, $\langle 0\,1\,1 \rangle_\gamma // \langle 1\,1\,1 \rangle_\alpha$), it can be seen that with the dynamic recrystallization progressing, $\langle 0\,1\,1 \rangle_\gamma$ preferentially orientated to the compressive direction.

Orientation distribution function (ODF) sections ($\varphi_2 = 45°$) of the longitudinal sections for the specimens deformed at 1100 °C with different strain rates are shown in Fig. 7. At 1 s^{-1}, the martensite shows strong $\{1\,10\}_{\alpha'} < 1\bar{1}1 >_{\alpha'}$ and $\{1\,10\}_{\alpha'} < 3\bar{3}1 >_{\alpha'}$ components. $\{1\,10\}_{\alpha'} < 1\bar{1}0 >_{\alpha'}$ and $\{1\,12\}_{\alpha'} < 11\bar{1} >_{\alpha'}$ components are dominant as the strain rate is 0.1 s^{-1}. The martensite shows similar texture characteristics under 0.01 s^{-1} and 0.001 s^{-1}, exhibiting $\{1\,10\}_{\alpha'} < 1\bar{1}0 >_{\alpha'}$, $\{1\,10\}_{\alpha'} < 1\bar{1}2 >_{\alpha'}$ and $\{1\,12\}_{\alpha'} < 1\bar{1}0 >_{\alpha'}$ components. It is well known that the crystallographic orientation of the parent austenite affects the specific crystallographic orientation of the martensite, owing to their K-S orientation relationship. Moreover, the morphology of austenite grains, the slip activity and the residual stress can also contribute to the martensite variant selection [26]. According to Mesplont and Cooman [27], the $\{1\,10\}_{\alpha'} < 1\bar{1}1 >_{\alpha'}$ and $\{1\,10\}_{\alpha'} < 3\bar{3}1 >_{\alpha'}$ components in this work at 1 s^{-1} should be originated from $\{1\,23\}_\gamma < 634 >_\gamma$ deformed austenite texture. The $\{1\,23\}_\gamma < 634 >_\gamma$ texture can also contribute to the $\{1\,10\}_{\alpha'} < 1\bar{1}0 >_{\alpha'}$ at 0.1 s^{-1}. Moreover, at 0.01 and 0.001 s^{-1}, both the $\{1\,10\}_{\alpha'} < 1\bar{1}0 >_{\alpha'}$ and $\{1\,12\}_{\alpha'} < 1\bar{1}0 >_{\alpha'}$ components may derive from $\{1\,12\}_\gamma < 111 >_\gamma$ deformed austenite texture.

The $\{1\,10\}_{\alpha'} < 1\bar{1}2 >_{\alpha'}$ component should be caused by $\{1\,10\}_\gamma < 112 >_\gamma$ deformed austenite texture. Even though the dynamic recrystallization is becoming prevailing with the strain rate decreasing, the strong $\{1\,00\}_{\alpha'} < 001 >_{\alpha'}$ components resulted from $\{1\,00\}_\gamma < 001 >_\gamma$ recrystallized austenite texture are not observed, indicating that the deformed austenite plays significant role in martensite texture evolution. Different strain rates could affect the austenite morphology, and it was reported that the aspect ratio of pancaked grains played important role in favoring selection of the transformed $\{311\}_\alpha < 011 >_\alpha$ and $\{2\,11\}_\alpha < 011 >_\alpha$ components [27].

3.3 Oxide Nanoparticles

Figure 8 shows the TEM images of the steels prior to hot deformation. The steel is characteristic of martensite laths and small amount of ferrite. Owing to the slowing cooling rate in consolidation stage, $M_{23}C_6$ carbides can be precipitated along lath boundaries, as highlighted by white arrows in Fig. 8a. It is interesting to note that some oxide nanoparticles have a "cap", as indicated by yellow arrows in Fig. 8. The nanocap appears on the one side of an oxide particle. Even for the oxide nanoparticles within the same grain, the relative positions of nanocaps to different oxide particles are different. Detailed characterization on these cap-shaped oxide particles will be shown in the following parts.

Figure 9a and b respectively show the martensite of the specimens deformed at 1100 °C with strain rates of 1 and 0.01 s^{-1}. Although some martensite laths can be observed,

Fig. 8 TEM images showing microstructure of the as-HIPed ODS steel under **a** low and **b** high magnification times
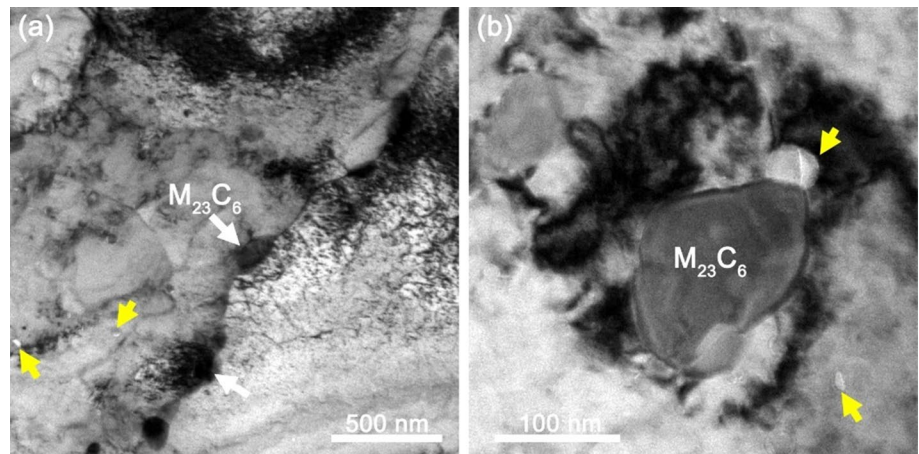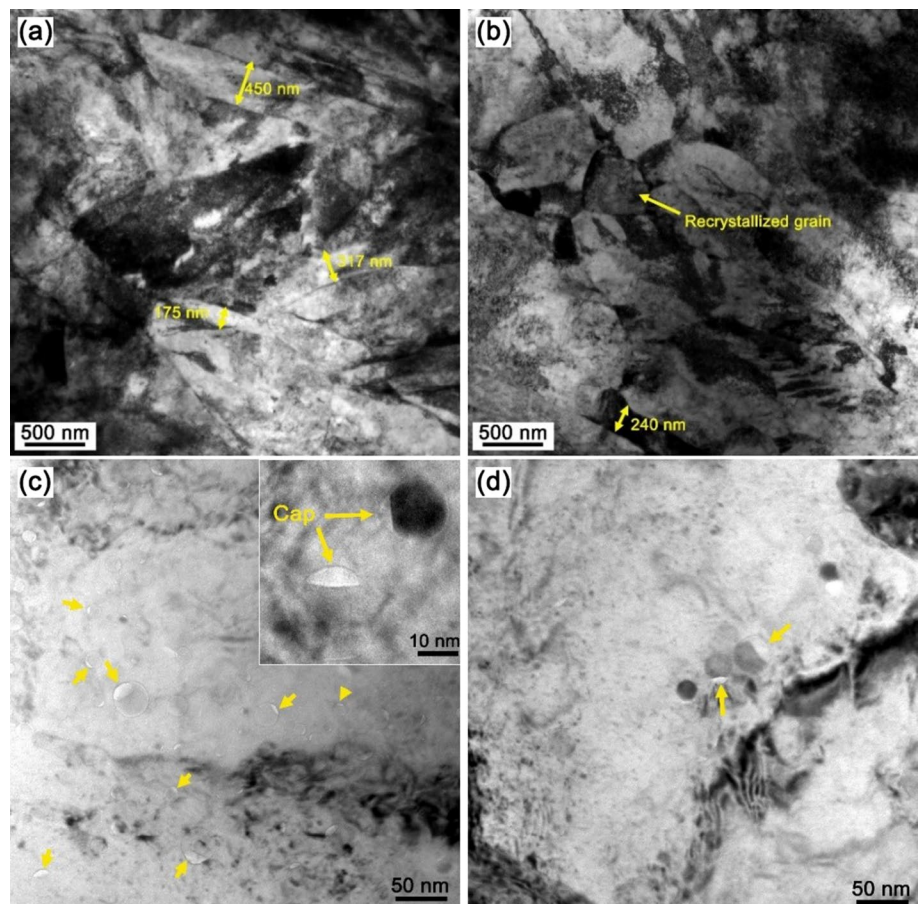

Fig. 9 TEM images showing martensite and oxide particles in the specimens deformed at 1100 $^{\circ}$C with strain rates of **a**, **c** 1 s^{-1} and **b**, **d** 0.01 s^{-1}

the martensite with bulk morphology is easier to be found. As shown in Fig. 9b, the recrystallized prior austenite grain has a size of about 500 nm, without exhibiting lath morphology of martensite. No significant difference in martensite size between these two specimens is identified. In the hot deformed specimens, the cap-shaped oxide nanoparticles can still be found, as shown in Fig. 9c and d. Figure 10 shows the HRTEM images of cap-shaped oxide nanoparticles in the

specimens deformed at 1100 $^{\circ}$C with the strain rate of 1 s^{-1}. The oxide nanoparticles shown in Fig. 10a and b respectively have sizes of 63 nm and 57 nm. As shown in Fig. 10a, FFT spots of both the particle (region A) and the nanocap (region B) can be obtained, indicating that the nanocap is still crystalline. However, it should be noted that the lattice of the nanocap (region B) is quite unclear. The transition region between the particle body and nanocap is disordered
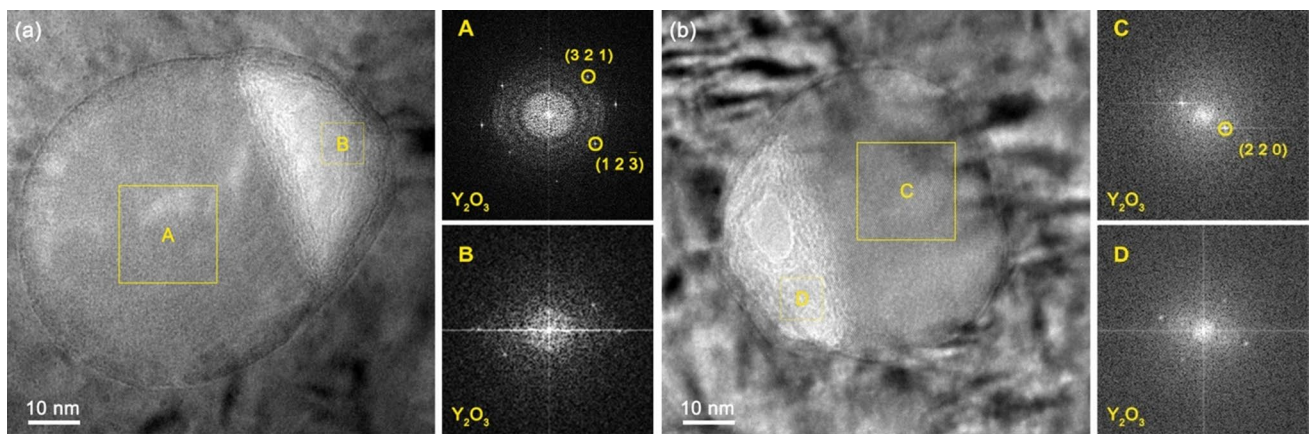
Fig. 10 HRTEM images and corresponding FFT patterns of cap-shaped oxide nanoparticles in the specimens deformed at 1100 °C with strain rates of 1 s^{-1}
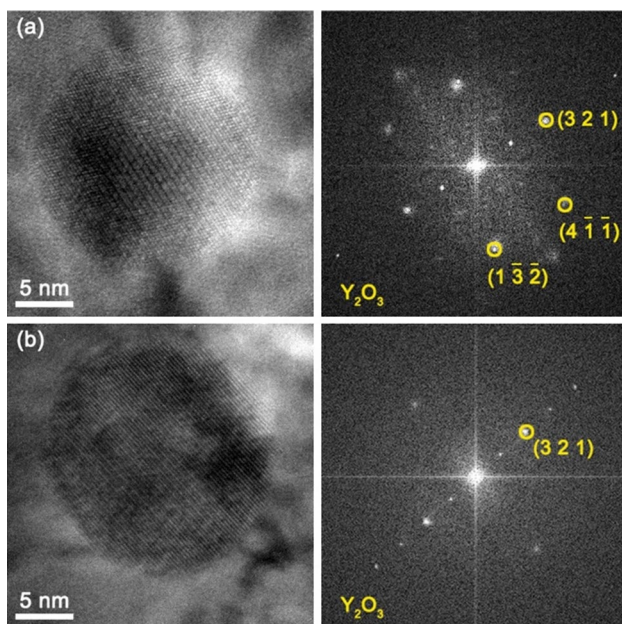

Fig. 11 HRTEM images and corresponding FFT patterns of slightly deformed oxide nanoparticles in the specimens deformed at 1100 °C with strain rates of **a** 1 s^{-1} and **b** 0.01 s^{-1}

and amorphous. These statements are also applicable for the particle shown in Fig. 9b. For comparison, Fig. 11 shows the HRTEM images of oxide nanoparticles with negligible deformation. The particle sizes shown in Fig. 11a and b are respectively 18.5 and 19 nm, and both of them exhibit better sphericity degree than those shown in Fig. 10.

Figure 12 shows the TEM images of the ODS steels deformed under 1000 °C/1 s^{-1} and 1150 °C/0.001 s^{-1} conditions. Voids are highlighted by yellow arrows. In Fig. 12b, it can be seen that voids are located at the large-sized oxide nanoparticles. The compressed large-sized oxide particles

with cap-shaped morphology are shown in Fig. 13a. From the HADDF image shown in Fig. 13b, it can be clearly seen that the cap parts exhibit lower contrast than the rest part of the particles, as indicated by yellow arrows in Fig. 13b, meaning that the cap parts has much smaller amounts of alloying elements than the rest part. This can also be confirmed by the elemental maps shown in Fig. 13c. Figure 14 shows the characteristics of cap-shaped oxide particles with medium size and minor deformation. These particles are still nearly spherical. The distribution of alloying elements within these particles is similar to that shown in Fig. 13. Alloying elements are depleted within the cap parts of cap-shaped oxide particles.

For the cap-shaped oxide particles shown in Fig. 10, the cap parts are disordered and amorphous. But the cap part of the particle shown in Fig. 15a exhibits crystalline structure, as shown in Fig. 15b. The region 2 corresponds to the cap part, having clear lattice structure. Yet the disordered regions can still be found in the region 2, as circled in Fig. 15b. Based on the FFT pattern shown in Fig. 15c and d, it is found that both of the regions 1 and 2 can be identified to be Y_2O_3. The $(1\ \bar{3}\ \bar{2})$ planes of regions 1 and 2 have a few degrees of deviation. Figure 16 shows the enlarged images for different parts of one cap-shaped oxide particle. For the top and lower right caps, the structures are amorphous. For the lower left cap, the lattice is quite unclear, but it can still be distinguished.

Based on the element distribution and lattice structure of cap-shaped oxide particles, it is suggested that the formation of cap-shaped particles should experience the following stages. The alloying elements within one side of the oxide particle starts to lose, but the crystal structure can still be retained. With the loss of alloying elements increasing, the crystal structure cannot be remained, producing amorphous structure. The amorphous structure may finally evolve into

Fig. 12 TEM images of the ODS steels deformed under **a** 1000 °C/1 s^{-1} and **b** 1150 °C/0.001 s^{-1}
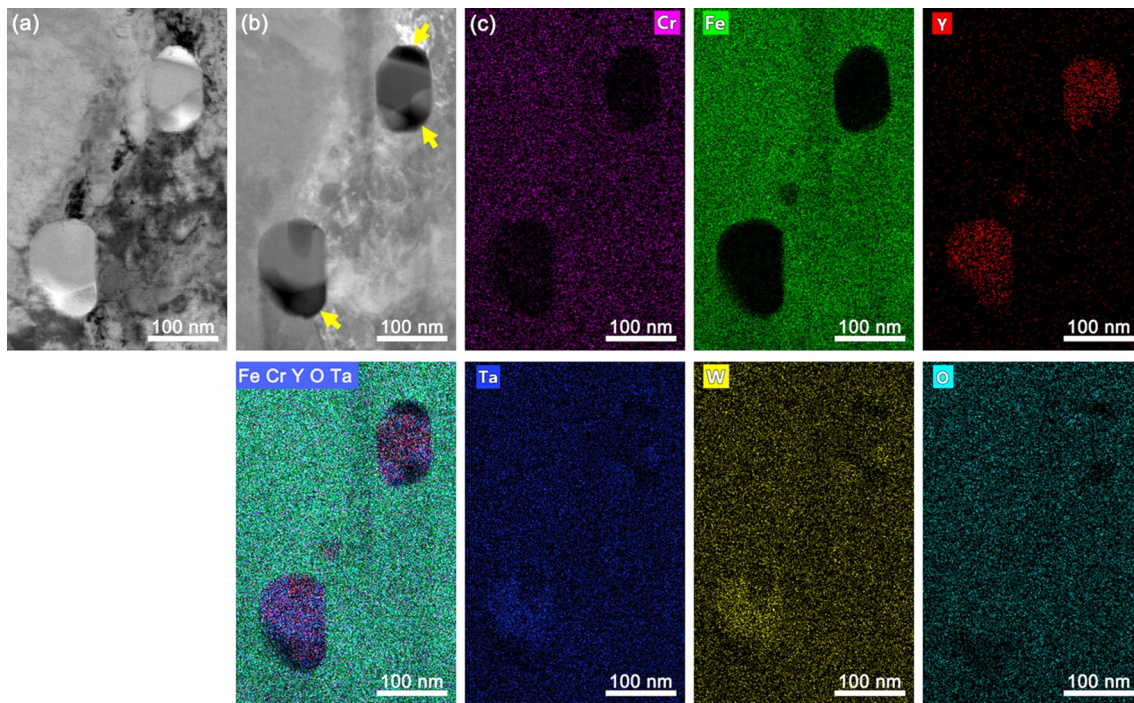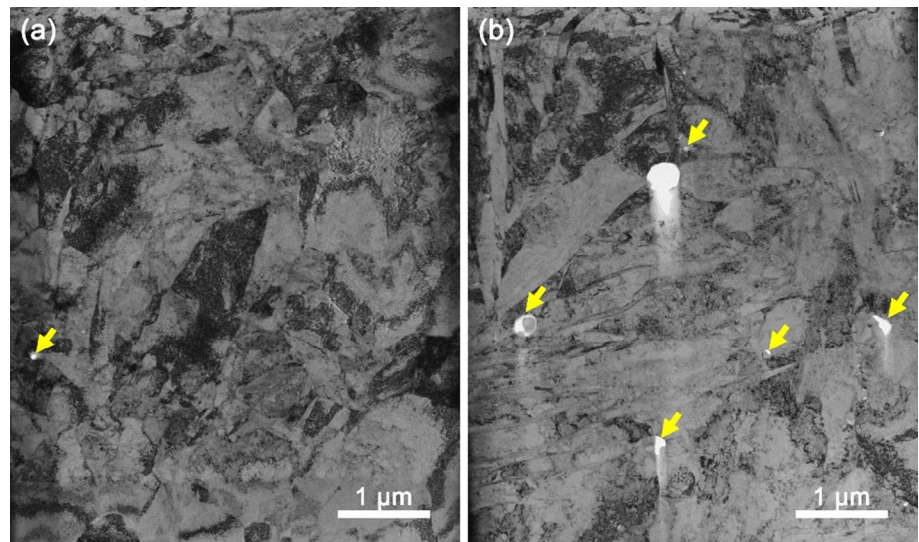

Fig. 13 **a** Bright-field and **b** HADDF images of the large-sized cap-shaped oxide particles in the steel deformed at 1150 °C with the strain rate of 0.001 s^{-1}, as well as **c** the corresponding elemental profiles

voids. To best knowledge, studies on these cap-shaped oxide nanoparticles have not been reported yet. The key factor to cause the loss of alloying elements within oxide nanoparticles is still unclear. It is possible that the interaction between the interface/dislocations and oxide particles leads to the depletion of alloying elements within oxides. When the interfaces or dislocations pass through the oxide particles, the contact part between the interfaces/dislocations and oxide particles may facilitate the diffusion of alloying elements within oxide nanoparticles, causing the loss of alloying elements within oxides.

Zhang and Pantleon investigated the response of oxide nanoparticles in ferritic PM2000 steel to dynamic plastic deformation at the room temperature [23]. It was reported that YAP oxide nanoparticles with sizes smaller than 20 nm experienced appreciable deformation, while particles larger than 20 nm were seldom deformed. Deformation-induced YAP to YAH transformation was suggested to be the main

Fig. 14 a Bright-field and **b** HADDF images of the medium-sized cap-shaped oxide particles in the steel deformed at 1150 °C with the strain rate of 0.001 s^{-1}, as well as **c** the corresponding elemental profiles
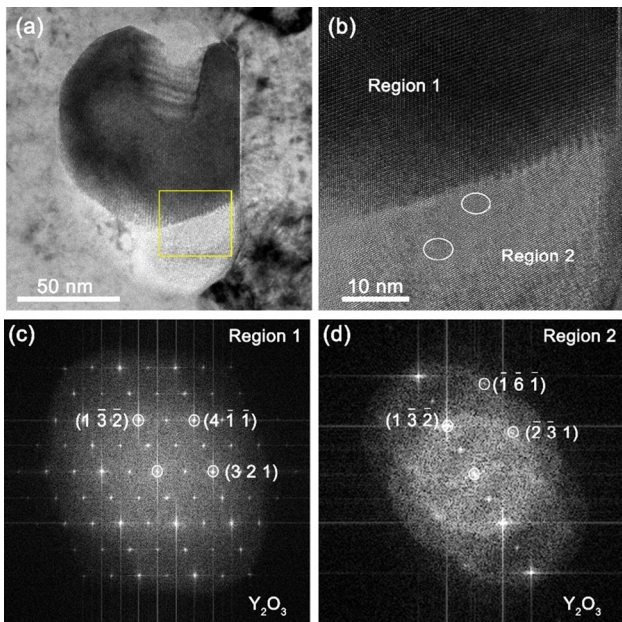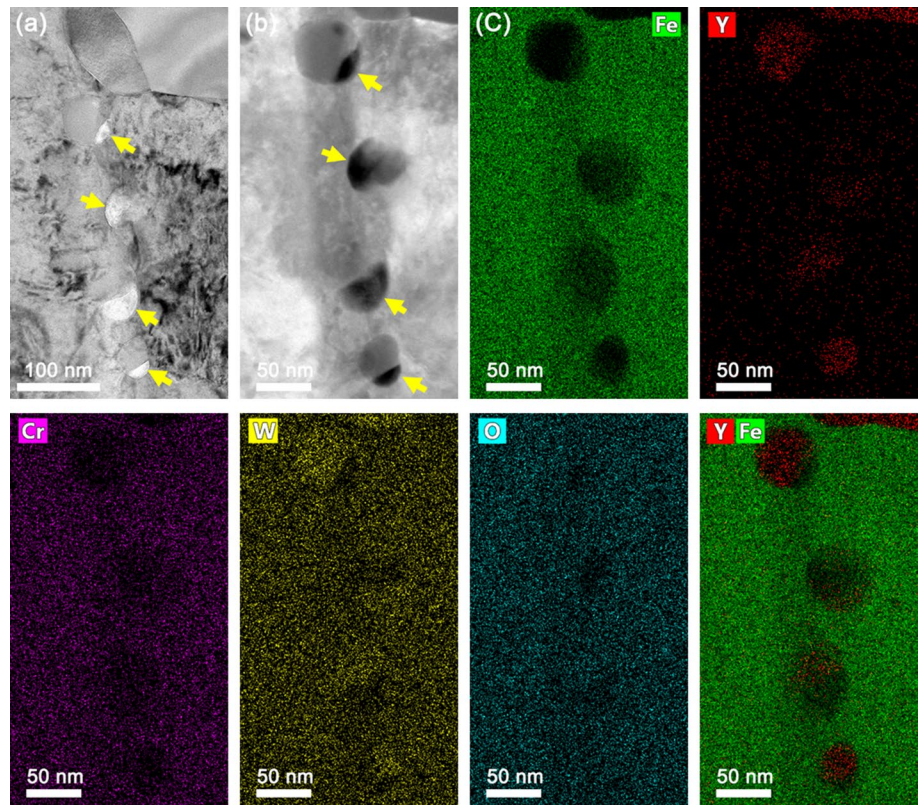

Fig. 15 a Bright-field image of the cap-shaped oxide particles in the steel deformed at 1150 °C with the strain rate of 0.001 s^{-1}, **b** the enlarged image of the rectangular area in **a**, **c** FFT pattern of the region 1 in **b** and FFT pattern of the region 2 in **b**
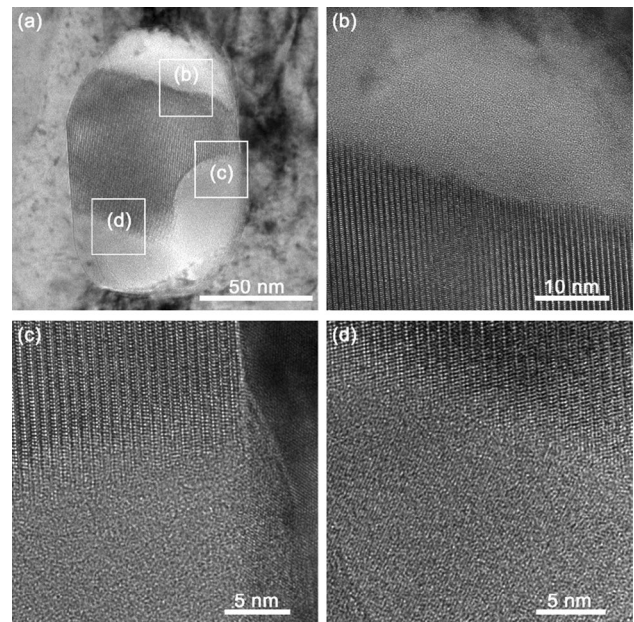

Fig. 16 a Bright-field image of the cap-shaped oxide particles in the steel deformed at 1150 °C with the strain rate of 0.001 s^{-1}, **b c d** the corresponding enlarged images of the rectangular areas in **a**

deformation mechanism for YAP nanoparticles larger than 20 nm, in contrast to the twining-dominated deformation mechanism of smaller particles [23]. However, in this work, it seems that the larger particles are more prone to be deformed than the smaller particles, as shown in Fig. 13. Maintaining deformation compatibility between Y_2O_3 particles (body-centered cubic) and austenite matrix should be the key reason for the plastic deformation of the nanoparticles. Compared with small oxide particles, the large-sized particles would produce more deformation to accommodate the surrounding matrix. As the stress level of austenite matrix around oxide nanoparticles is large enough, sufficient stresses will be imposed on oxide nanoparticles, leading to the deformation of oxide nanoparticles. But the deformation strain of oxide nanoparticles is always below the macroscopic applied strain. On the other hand, small oxide particles are easier to produce coherent or semi-coherent interface between oxide and austenite, and then the interface strength between smaller particles and austenite is stronger.

Although oxide nanoparticles are deformed upon the hot deformation, the PLC effects discussed in Sect. 3.1 is still suggested to be related to the solute-dislocation interaction. In this work, cap-shaped oxide particles with alloying elements depletion within the cap parts exist in the as-fabricated and hot deformed steels. More dislocations will pass through oxide particles at higher strain rates. If the formation of cap-shaped oxides is indeed related to the interactions between interface/dislocations and oxides, this interaction should be enhanced at high strain rates. More alloying elements from the oxide particles will be released into the matrix to pin dislocations. On this sense, the explanation can be consistent with the results shown in Fig. 4. Values of stress change at 1 s^{-1} are larger than those at 0.1 and 0.01 s^{-1}. On the other hand, the cap part between the cap-shaped oxide particles and matrix should be one weak connection, considering the element depletion within the cap parts. Nanovoids can be easier produced at these weak connections when the strain rates are high. The nanovoids can also promote the diffusion of solute atoms within the matrix to pin moving dislocations.

4 Conclusions

The flow behaviors and microstructure evolution of 9Cr ODS steels upon hot deformation are investigated, and it is found that the Portevin-LeChatelier effect and microstructure characteristics of 9Cr ODS steels are closely related to the strain rates. The main findings can be summarized as follows:

1. The flow stress of 9Cr ODS steels upon hot deformation is characteristics of type B serrations, with respect to the strain rates of 0.01, 0.1 and 1 s^{-1}. The PLC effect is sensitive to the strain rate, but not to the deformation temperature. With the deformation temperature and strain rate increasing, the critical strain for PLC effect decreases, and the stress drops at 1 s^{-1} are quite larger than those at 0.01 and 0.1 s^{-1}.

2. With the strain rate decreasing, both dynamic recovery and recrystallization of austenite grains are enhanced, affecting the austenite morphology and the subsequent martensite formation. As the strain rate decreases from 1 to 0.001s^{-1}, $<1\,1\,1>_\alpha$ direction preferentially orientates to the compressive direction. The local martensite texture of ODS steels along longitudinal sections is closely related to the deformed austenite texture components.

3. Cap-shaped oxide particles are found in the as-fabricated and hot deformed 9Cr ODS steels. The cap parts of the cap-shaped oxide particles are characteristics of alloying element depletion, and their crystal structure can be either crystalline or amorphism. Larger oxide particles are more prone to be deformed than smaller particles, and voids can be found at the interface between the large-sized oxide and the matrix.

Declarations

Conflict of interest The authors declare that they have no known competing financial interests or personal relationships that could have appeared to influence the work reported in this paper.

References

1. X. He, J. Song, J. Tan, B. Zhang, H. Xia, Z. He, X. Zhou, M. Zhao, X. Liu, L. Xu, Bai. SiC coating: an alternative for the protection of nuclear graphite from liquid fluoride salt. J. Nucl. Mater **448**(1), 1–3 (2014)

2. C.M. Parish, R.M. White, J.M. LeBeau, M.K. Miller, Response of nanostructured ferritic alloys to high-dose heavy ion irradiation. J. Nucl. Mater **445**(1), 251–260 (2014)

3. G.R. Odette, M.J. Alinger, Wirth. Recent developments in irradiation-resistant steels. Annu. Rev. Mater. Sci **38**(1), 471–503 (2008)

4. H.S. He, L.M. Yu, C. Liu, H. Li, Q. Gao, Yongchang Liu, Research progress of a novel martensitic heat-resistant steel G115. Acta Metall. Sin **58**(3), 311–323 (2022)

5. M. Nagini, R. Vijay, K.V. Rajulapati, K.B.S. Rao, M. Ramakrishna, A.V. Reddy, G. Sundararajan, Effect of process parameters on microstructure and hardness of oxide dispersion strengthened 18Cr ferritic steel. Metall. Mater. Trans. A **47**(8), 4197–4209 (2016)

6. X. Zhou, H. Chen, C. Liu, Y. Liu, Residual ferrite control of 9Cr ODS steels by tailoring reverse austenite transformation. Acta Metall. Sin. (Engl. Lett.) **34**(2), 187–195 (2021)

7. X. Zhou, G. Li, X. Shen, Y. Liu, Tensile strength improvement of martensitic ODS steels with zr and hf additions. Mater. Sci. Eng. A **829**, 142071 (2022)

8. X. Liu, J. Wang, Y. Li, S. Li, Q. Cai, Densification mechanism of Ti-Al-Nb alloys pressurelessly sintered from Al-Nb master alloy powder for cost-effective manufacturing. J. Alloys Compd. **936**, 168307 (2023)

9. R. Jarugula, S. Koppoju, R. Jeyaraam, S. Ganesh Sundara Raman, G. Sundararajan, On the understanding of microstructural evolution during hot deformation of n-ODS-18Cr ferritic steel containing heterogeneous microstructure. Mater. Sci. Eng. A **800**, 140343 (2021)

10. D.L. Sornin, A. Karch, R.E. Logé, Competition between intragranular and intergranular deformation mechanisms in ODS ferritic steels during hot deformation at high strain rate. J. Mater. Sci **53**(4), 2965–2975 (2018)

11. Y. Zhang, J.P. Liu, S.Y. Chen, X. Xie, P.K. Liaw, K.A. Dahmen, J.W. Qiao, Wang. Serration and noise behaviors in materials. Prog. Mater. Sci **90**, 358–460 (2017)

12. G. Zhang, Z. Zhou, H. Sun, L. Zou, M. Wang, S. Li, Hot deformation behavior and processing map of a 9Cr ferritic/martensitic ODS steel. J. Nucl. Mater. **455**(1), 139–144 (2014)

13. M.K. Dash, S. Saroja, R. John, R. Mythili, A. Dasgupta, EBSD study on processing domain parameters of oxide dispersion strengthened 18Cr ferritic steel. J. Mater. Eng. Perform. **28**(1), 263–272 (2019)

14. Y. Shao, L.M. Yu, Y.C. Liu, Z.Q. Ma, H.J. Li, J.F. Wu, Hot deformation behaviors of a 9Cr oxide dispersion-strengthened steel and its microstructure characterization. Int. J. Miner Metall. Mater. **26**(5), 597 (2019)

15. P. Hähner, On the critical conditions of the Portevin-Le Châtelier effect. Acta Mater. **45**(9), 3695–3707 (1997)

16. X.M. Chen, Y.C. Lin, D.X. Wen, J.L. Zhang, M. He, Dynamic recrystallization behavior of a typical nickel-based superalloy during hot deformation. Mater. Design. **57**, 568–577 (2014)

17. K. Gopinath, A.K. Gogia, S.V. Kamat, U. Ramamurty, Dynamic strain ageing in Ni-base superalloy 720Li. Acta Mater. **57**(4), 1243–1253 (2009)

18. Y. Cai, C. Tian, G. Zhang, G. Han, S. Yang, S. Fu, C. Cui, Q. Zhang, Influence of γ′ precipitates on the critical strain and localized deformation of serrated flow in Ni-based superalloys. J. Alloys Compd. **690**, 707–715 (2017)

19. X. Wang, G. Han, C. Cui, S. Guan, J. Li, G. Hou, Y. Zhou, X. Sun, On the γ′ precipitates of the normal and inverse Portevin-Le Châtelier effect in a wrought Ni-base superalloy. J. Mater. Sci. Technol. **35**(1), 84–87 (2019)

20. J. Mola, G. Luan, Q. Huang, C. Ullrich, O. Volkova, Y. Estrin, Dynamic strain aging mechanisms in a metastable austenitic stainless steel. Acta Mater. **212**, 116888 (2021)

21. B.H. Tian, Y.G. Zhang, C.Q. Chen, Abnormal flow behavior and serrated flow in Al–Li single crystals. Mater. Sci. Eng. A **247**(1), 263–269 (1998)

22. S. Kumar, Inverse behaviour of the onset strain of serrated flow. Scr. Metall. Mater. **33**(1), 81–86 (1995)

23. Z. Zhang, W. Pantleon, Response of oxide nanoparticles in an oxide dispersion strengthened steel to dynamic plastic deformation. Acta Mater. **149**, 235–247 (2018)

24. E. Pink, H. Weinhandl, The distribution of stress-drop sizes in serrated flow of an aluminium alloy and a mild steel. Scripta Mater. **39**(9), 1309–1316 (1998)

25. J.M. Reed, M.E. Walter, Observations of serration characteristics and acoustic emission during serrated flow of an Al–Mg alloy. Mater. Sci. Eng. A **359**(1), 1–10 (2003)

26. R.K. Ray Jonas, Transformation textures in steels. Int. Mater. Rev **35**(1), 1–36 (1990)

27. C. Mesplont, B.C. De Cooman, Effect of austenite deformation on crystallographic texture during transformations in microalloyed bainitic steel. Mater. Sci. Technol. **19**, 875–886 (2003)